Digital Beamforming for Spaceborne Reflector-Based Synthetic Aperture Radar Part 2: Ultra-Wide Swath Imaging Mode

Marwan Younis, *Fellow, IEEE,* Felipe Queiroz de Almeida, Michelangelo Villano, *Senior Member, IEEE,* Sigurd Huber, Gerhard Krieger, *Fellow, IEEE,* Alberto Moreira, *Fellow, IEEE*

***Abstract*—Utilizing digital beamforming techniques in conjunction with the feed array of large deployable reflector antennas can boost the performance of synthetic aperture radar (SAR) systems. Multi-channel SAR overcomes the constraints of classical single-channel SAR allowing for wide-swath imaging at fine azimuth resolution. Part 1 of this tutorial provided an introduction to the instrument structure of a digital beamforming (DBF) imaging radar and the particularities/variants of its basic operation mode, known as a single-beam scan-on-receive (SCORE) system.**

The underlying part 2 of the tutorial paper addresses the topic of ultra-wide swath imaging in the order of a few hundred kilometers, enabled through DBF. A detailed insight into simultaneous multiple sub-swath imaging is given; gaps (blind ranges) that occur in this operation mode are addressed; and the data streams management at the various on-board processing stages is explained, put in relation to the imaging mode, and expressions for the data rates are provided.

A further beamforming topic seized in part 2 of this tutorial trilogy is the feed array excitation (complex weights) and the resulting primary and secondary radiation patterns. This is explained in the context of a reference reflector-feed antenna system providing numerous example cases aiming to foster the understanding of the topic.

***Index Terms*—synthetic aperture radar (SAR), digital-beam forming, reflector-based SAR.**

I. Introduction

The scan-on-receive (SCORE) imaging technique described in the first part of the tutorial [1] generates a narrow, time-variant, and high-gain receive beam (antenna radiation pattern) that follows the reflected radar echo traversing the ground. In its basic implementation, SCORE improves the signal-to-noise ratio and suppresses the range ambiguities, but it does not allow for a substantial increase of the imaged swath width beyond a few tens of kilometers. The latter deficiency is significant, as one of the crucial parameters of spaceborne SAR systems monitoring dynamic processes is the width of the imaged swath. A wide swath enables reducing the revisit time, shortening the time between successive observations of any ground region and by this facilitates the monitoring of dynamic processes. Current in-orbit operational SAR system image swaths in the order of $20\,\mathrm{km}$ to $80\,\mathrm{km}$ in stripmap imaging mode. Although the imaged swath width of conventional single-channel SAR may be increased by utilizing burst operation modes such as ScanSAR or TOPS [2], [3], this increase is paid for by a degraded azimuth resolution.

The multi-beam SCORE digital beamforming technique detailed in this paper can overcome the above mentioned dilemma allowing for simultaneous high-resolution and wide-swath SAR [4], [5], [6]. Multi-beam SCORE may be understood as an intrinsic stripmap-based imaging mode allowing for ultra-wide swath with no difference for the SAR image processing. It is an extension to the basic SCORE technique suggested in [7], [8], [9]. Multi-beam SCORE is the reference operation mode of the NISAR mission by NASA/ISRO [10], [11], [12] and is also implemented by JAXA for the ALOS-4 mission [13] as well as by ESA for the ROSE-L mission [14]. Further, multi-beam SCORE operation, is inherent to the staggered SAR mode, cf. [15], [16] and part 3 of the tutorial paper, which has been considered for other missions (and mission proposals) such as NISAR and Tandem-L [17], [18], [19], [11].

To explain the innovative SAR technique required for ultra-wide swath imaging a reference SAR system capable of imaging a swath of $355\,\mathrm{km}$ (ground range) is considered. The parameter values of this system are developed in a step-by-step procedure throughout the paper explaining the beamforming approach and relating it to the instrument operation.

The overall structure of the paper is as follows: In the following section the impact of imaging a wide swath on the radar echo timing is analyzed. Next an operation mode, known as multi-beam SCORE, capable of imaging an ultra-wide swath is detailed. The reflector-based beamforming underlying the imaging mode is elaborated in section V giving examples for the excitation, the resulting reflector illumination (primary beam) and the resulting secondary radiation pattern. Multi-Beam SCORE introduces gaps in the imaged swath caused by the transmit pulse instances of the instrument; this issue is analyzed in detail section VI where the expressions governing the extent of the gaps are derived. Last but not least the effort for data stream handling and memory management is discussed and related to basic SAR performance parameters such as resolution and oversampling.

II. An Ultra-Wide Swath imaging System

In the following the consequences of extending the swath width on the timing are discussed; it is shown that the single-beam SCORE technique is not suitable for ultra-wide swath

All authors are with the Microwaves and Radar Institute of the German Aerospace Center (DLR), Germany. Marwan Younis and Alberto Moreira are also with the Karlsruhe Institut für Technologie (KIT). Gerhard Krieger is also with the Friedrich-Alexander-Universität Erlangen-Nürnberg (FAU)

imaging and therefore needs to be enhanced utilizing digital beamforming.

Starting point is the timing analysis shown in Fig. 1 with three sub-swaths (orange bars) imaged at a PRF of 1770 Hz. The timing (or diamond) diagram shows the transmit pulse instances (blue strips) and nadir returns (green strips) versus a range of PRF values (abscissa). These are related to the geometrical swath parameters, here the incidence and off-nadir look angle (ordinate). It is used to visualize possible positions for the echo window and allows the system engineer to decide on the number, placement and extent of the imaged sub-swaths. The PRF has been chosen higher than the minimum value determined by (1) in [1].

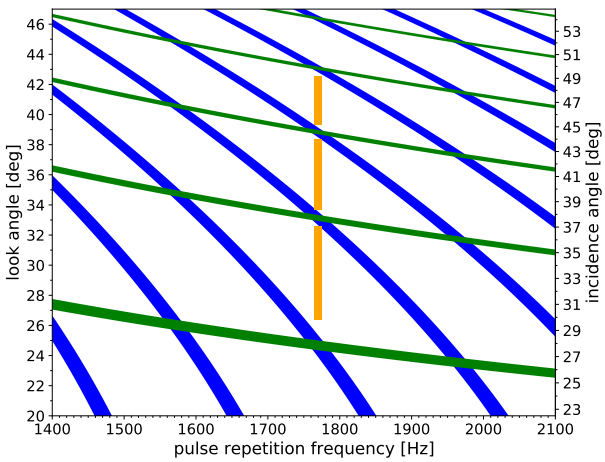

Figure 1: Timing diagram for a SAR operating from a 760 km orbit. The blue and green strips depict the transmit events and nadir echo return, respectively, while the imaged swaths are indicated by the orange bars at $f_{\text{prf}} = 1770\,\text{Hz}$.

Parameter Values: The timing diagram in Fig. 1 is for a SAR imaging a swath of 30° to 49° incidence angle range corresponding to a slant range of $R_{far} - R_{near} \approx 228\,\text{km}$. For the pulse repetition interval of $T_{\text{pri}} = 565\,\mu\text{s}$ and a pulse duty cycle of 6 % the pulse duration becomes $\tau_p \approx 34\,\mu\text{s}$. According to (2) in [1] this results in a ground echo return time of $T_{echo} = 1.52\,\text{ms}$.

The example above is a typical scenario for ultra-wide swath imaging, where the time duration of the ground return, T_{echo}, is larger than the time T_{pri} between two transmitted pulses as shown in Fig. 2. This can also be deduced from the timing diagram as the sub-swaths are "interrupted" by transmit events; for the case shown in Fig. 1 there are two such transmit events.

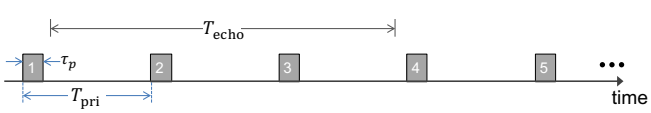

Figure 2: Transmit pulse sequence versus time (not to scale). Here, the duration of the ground echo return, T_{echo}, is larger than the available receive window $T_{\text{pri}} - \tau_p$, between the transmit pulses.

The consequences of the above are twofold:

- As multiple pulses are transmitted within the swath echo time T_{echo}, it is obvious that these traverse the swath simultaneously. Their temporal separation, T_{pri}, maps into different slant range distances $T_{\text{pri}} \cdot c/2$ with c the speed of light. In a conventional, i.e., a non-DBF system, these echoes would be considered unwanted range ambiguities, but here they are desired (useful) SAR echo signals.
- The reception of the ground echo will be interrupted by transmit events. This is a consequence of a monostatic system where the same antenna and front-end hardware are used for transmission and reception; since the hardware cannot transmit and receive at the same time, the two events are interleaved. With the time-to-range mapping, namely $t = 2r/c$, these interruptions mask the reception of the echo of a specific range segment which results in imaging gaps.

III. Multi-Beam SCORE

The multi-beam SCORE utilizes a single wide transmit beam illuminating the whole imaged swath, and multiple receive SCORE beams scanning the reflected echo signals traversing the ground [7], [20], [8] as shown in Fig. 3. The multi-beam operation in elevation means that several echo signals arrive at the same time from different directions, where, in a reflector-feed antenna system, each echo activates a different set of feed antenna elements. Using the same terminology developed in [1], DBF can then be understood as combining the signals from a set of feed elements yielding N_{beam} output data streams. These are represented by $b_k[l]$, where k is the output data stream index and l the discrete time sample index. As the direction of arrival is changing with time the secondary beams need to scan the swath which manifests itself by the time-dependent complex DBF weights. Using vector notation, N_{beam} simultaneous data streams $\mathbf{b}_k, k = 1, \ldots, N_{beam}$ are generated each corresponding to one SCORE beam.

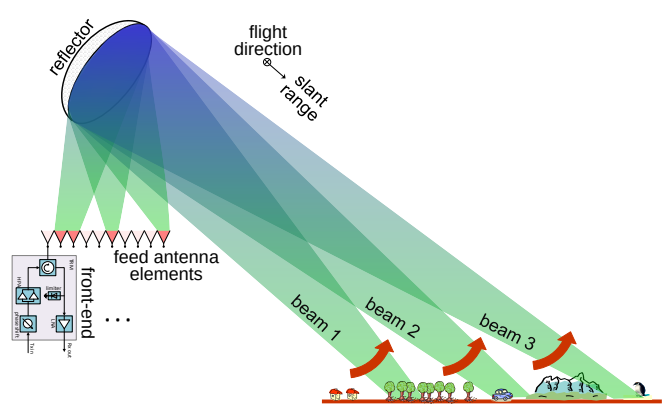

Figure 3: The multi-beam SCORE operation mode where multiple simultaneous beams scan the signal echo traversing the ground.

The range-time diagram for multi-beam SCORE is shown in Fig. 4a. Due to the increased swath, several echo signals arrive simultaneously from different ranges; there are, for

example, three echoes shown at time $t = t_1$ in the figure. As mentioned previously, the beamforming units must create multiple simultaneous beams, which can also be understood as spatial filters separating the echoes into independent data streams. Obviously, imaging a wider swath provides for an increased information rate which manifests itself through a higher data rate. Note that this also requires a longer feed array and thus more feed elements (in elevation) to enable the extended angular scan range.

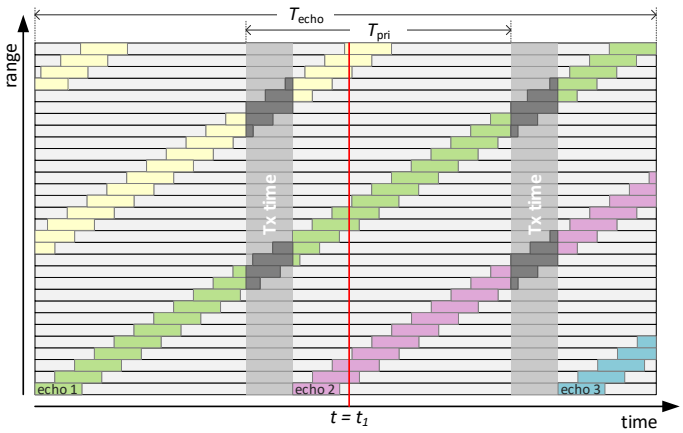

(a) range-time diagram

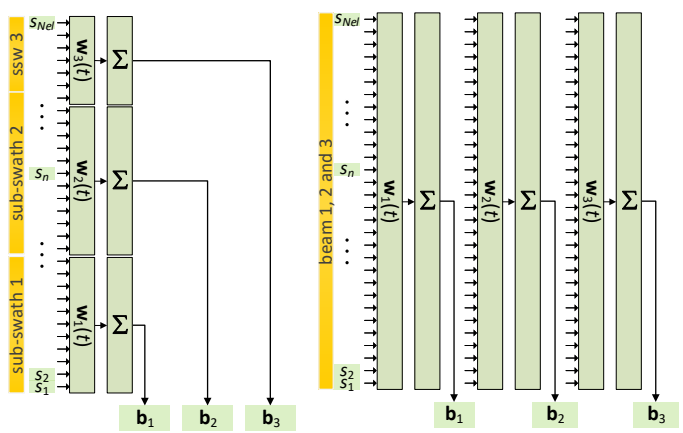

(b) partitioned swath DBF (c) concatenated swath DBF

Figure 4: Range-time diagram for ultra-wide swath imaging with the multi-beam SCORE such that multiple pulses (here three) traverse the swath simultaneously (a); and two alternative SCORE beamforming methods: partitioned swath, where each beam is assigned a segment of the swath (b), and concatenated swath, where the beams following the signal echo throughout the complete swath (c).

The number of beams N_{beam} to be formed simultaneously depends upon the system's PRF. The average number of elevation beams can be estimated by:

$$N_{beam} = \lceil T_{echo} \cdot f_{\text{prf}} \rceil \tag{1}$$

with the ceil operator $\lceil \cdot \rceil$, where $\lceil x \rceil$ maps x to the smallest integer greater than or equal to x. The exact number of beams may vary over time and is obtained from the detailed timing analysis [21]. This can be also understood as the mean number of pulses which are simultaneously traversing the ground (followed by the SCORE beams) during the reception of the full echo of duration T_{echo}.

Parameter Values: For a $f_{\text{prf}} = 1770\,\text{Hz}$ and $T_{echo} = 1.52\,\text{ms}$ the number of beams can be computed using (1) which results in $N_{beam} = 3$. The diamond diagram in Fig. 1 shows that three sub-swaths are required to image a $355\,\text{km}$ swath (look angle range from $26.4°$ to $42.5°$). The typical number of beams for reflector SAR is in the range of $N_{beam} = 3$ to 6.

This operation mode requires the receive signal vector to be multiplied by different sets of time-varying weights corresponding to different output beams. The received signal of feed element n is denoted as a column vector $\mathbf{s}_n$ and collected in the matrix $\mathbf{S}$. The weight vector that generates the k-th output is $\mathbf{w}_k(t) = [w_{1,k}(t), w_{2,k}(t), \ldots, w_{N_{el},k}(t)]^T$. With this the equations from tutorial part 1 are rewritten for the multi-beam SCORE:

$$\mathbf{b}_k = \mathbf{S}\mathbf{w}_k(t) = \sum_{\mathcal{N}_{act,k}} \mathbf{c}_{n,k} = \sum_{\mathcal{N}_{act,k}} \mathbf{s}_n w_{n,k}(t). \tag{2}$$

Here, $\mathcal{N}_{act,k}(t) = \{n_{0,k}(t), n_{0,k}(t)+1, \ldots, n_{1,k}(t)\}$ defines the active elements of beam k, and $\mathbf{c}_{n,k}$ is the weighted output signal of element n contributing to beam k.

The beam-to-swath mapping is not included explicitly in the above equation, i.e., the k-th beam is not related to any specific sub-swath. Instead the mapping is determined by the digital hardware topology. In the following two implementations of the multi-beam SCORE are discussed: partitioned swath SCORE and concatenated swath SCORE.

A. Partitioned Swath SCORE

A functional realization for the case that the sets of elements of the different beams do not overlap is illustrated schematically in Fig. 5a. Here, different beams do not share the same feed elements, thus the sets of active feed elements are disjunctive such that $\mathcal{N}_{act,i} \bigcap \mathcal{N}_{act,j} = \emptyset \ \forall i \neq j$. The configuration in the figure generates $N_{beam} = 3$ output beams corresponding to three sub-swaths.

The region (sub-swath) on the ground traversed by each beam is determined by the angular segment covered by the set of feed elements constituting that beam. This is because the hardware is implemented such that the output data stream of each functional sub-swath DBF Unit (ssw-DBFU) covers only part of the complete swath. The term "functional" is used because the actual hardware realization may still include several ssw-DBFUs in a single FPGA.

The association between the echo signals and the beamforming is best understood by relating the range-time diagram in Fig. 4a to the beamforming schematic in Fig. 4b: A single echo traversing the swath from near to far range would first be handled by ssw-DBFU 1, then later successively switched over to the units 2 and 3. In general, the echo of transmit pulse $i = 1, 2, \ldots$ is successively handled by ssw-DBFU $k = 1, 2, \ldots, N_{beam}$ where each ssw-DBFU covers one sub-swath and $\mathbf{b}_k$ is the k-th sub-swath output vector. The

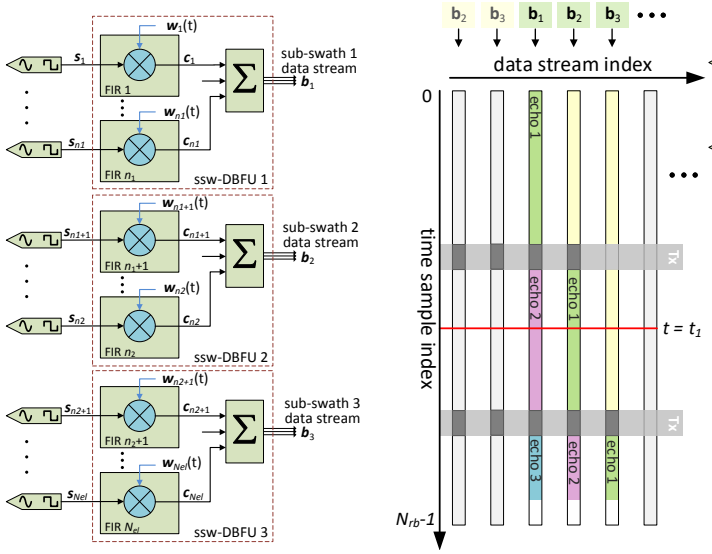

(a) functional sub-swath DBF unit (b) range-azimuth diagram

Figure 5: Partitioned swath SCORE technique for imaging a wide swath, where each output data stream corresponds to one sub-swath. The input range-time diagram is shown in Fig. 4a.

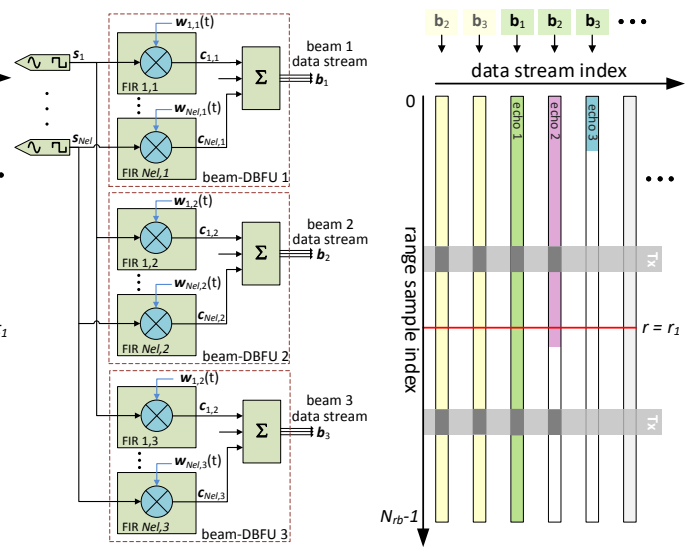

(a) functional beam DBF unit (b) range-azimuth diagram

Figure 6: Concatenated swath multi-beam SCORE technique for imaging an ultra-wide swath; each output data stream corresponds to the complete swath (for each transmitted pulse). The input range-time diagram is shown in Fig. 4a.

dimension (number of elements) of the weight vector of each DBF unit is less than the total number of antenna elements N_{el}. In the case of the three sub-swaths shown in Fig. 5a the weights are:

$$\begin{aligned}\mathbf{w}_1(t) &= [w_{1,1}(t), \ldots, w_{n_1,1}(t)]^T \\ \mathbf{w}_2(t) &= [w_{n_1+1,2}(t), \ldots, w_{n2,2}(t)]^T \\ \mathbf{w}_3(t) &= [w_{n_2+1,3}(t), \ldots, w_{N_{el},3}(t)]^T \end{aligned} \tag{3}$$

where $n_1 < n_2 < N_{el}$. Since multiple pulses traverse the ground simultaneously all ssw-DBFUs are active at any time instance, excluding the duration of transmit events.

The range-azimuth diagram in Fig. 5b shows the data after beamforming. The data from any single echo, e.g. green echo 1, are distributed over several columns. This is because the data stream of each column is generated by different ssw-DBFUs, or, stated differently, each column contains the data of different echoes. The ordinate of the range-azimuth diagram represents the time of the sample and *not* the range. The echo data of the complete swath (vs. range) are obtained by concatenating (re-ordering) the output data of the beamformer.

B. Concatenated Swath SCORE

The DBF implementation shown in Fig. 4c allows generating a SCORE beam that follows the ground echo over the complete swath interrupted by the transmit events. In this case the output signal vector $\mathbf{b}_k$ represents one range line of data from near to far range. An increased complexity in terms of hardware implementation results because each beam, scanning the ground from near to far range, ends up activating all N_{el} feed elements during the echo time T_{echo}. Further, at any instance of time the sets of active elements corresponding to different beams i and j may overlap, i.e., $\mathcal{N}_{act,i} \bigcap \mathcal{N}_{act,j} \neq \emptyset$.

To understand the functionality of the underlying beamforming the echo signal data of each feed element —at the output of the analog-to-digital converter (ADC)— is considered being split into N_{beam} data streams. Each data stream is multiplied by a different set of weights corresponding to one SCORE beam. The schematic shown in Fig. 6a connects each feed element data $\mathbf{s}_n$ to *all* beam-DBF Units (beam-DBFU). Thus, the output of each beam-DBFU is the weighted sum of N_{el} feed elements, and each feed element may contribute to all beams (compare to the ssw-DBFU in Fig. 5a).

Here, unlike partitioned swath SCORE, the output data stream $\mathbf{b}_k$ no longer corresponds to sub-swath k, but instead to the echo signal from the complete, i.e., concatenated, swath for each transmitted pulse. In Fig. 6b, the echo signal of each transmit pulse is mapped to one column of the range-azimuth diagram, the ordinate of which now represents the slant range. The notation used is such that the receive echo signal data stream of transmit pulse $i = 1, 2, \ldots$ is $\mathbf{b}_k$ where $k = (i-1) \bmod N_{beam} + 1$.

C. Dispersive Multi-Beam SCORE

Dispersive single-beam SCORE has been addressed in Part 1 of the tutorial. Extending the mathematical description of (24) and (28) in [1] to the multi-beam case is straightforward

and given by:

$$\mathbf{c}_{n,k} = \sum_{b=1}^{N_{sb}} \mathbf{s}_n^b w_{n,k}^b(t) = \sum_{b=1}^{N_{sb}} \mathbf{F}^b \mathbf{s}_n w_{n,k}^b(t)$$
$$= \left(\sum_{b=1}^{N_{sb}} \mathbf{G}_{n,k}^b(t) \right) \mathbf{s}_n = \mathbf{G}_{n,k}(t) \mathbf{s}_n \quad (4)$$

with $w_{n,k}^b(t)$ the time-changing weight of sub-band b for the receive signal of feed element n to generate output beam k. Note that the matrix subscripts n, k are used to indicate the dependency on the channel and output beam, respectively, and are not related to the matrix shape. The Toeplitz matrix $\mathbf{F}^b$ implementing the finite impulse response (FIR) bandpass filter is independent of the output beam and channel, whereas the band matrix $\mathbf{G}_{n,k}$ does depend on k and n, since it includes the beam dependent weights. In Fig. 5a and 6a the dispersive beamforming has already been suggested by labeling the multiplication units as FIR filters.

D. Partitioned versus. Concatenated Swath SCORE

Partitioned swath SCORE is the simplest realization to image an ultra-wide swath and requiring the least system resources and hardware, since the sub-swath concatenation is carried out on-ground and does not require on-board resources. The drawback of the configuration is that each ssw-DBFU has access to a fixed set of elements' data streams which limits the flexibility in changing the operation mode parameters. This inflexibility may be mitigated by a specific hardware implementation of the FPGAs to allow an overlap between the elements.

The advantage of concatenated swath SCORE is that each DBF unit has access to the data of all feed elements, which provides more flexibility for shaping the beams and a redundancy, for example, in case of element failure. Further, the output data streams, $\mathbf{b}_k$, represent range lines over the complete swath (excluding the blockage times due to transmit events) and are available for further on-board processing. As will be seen in tutorial Part 3, the latter is a prerequisite for azimuth filter on-board processing. The advantages come at the expense of a more elaborate digital network (hardware) and higher computational cost (number of operations per data sample); the added complexity is a non-negligible factor on the overall system cost.

IV. Azimuth Channels

Digital beamforming SAR commonly utilizes multiple digital channels both in azimuth and elevation. Here we extend the system description to consider also multiple azimuth channels. As the system is acquiring data simultaneously with N_{az} azimuth channels, the hardware structure for beamforming described previously needs to be repeated N_{az} times. Thus, each azimuth channel has a complete elevation hardware set consisting of front-ends, analog-digital-converters and DBF units. In general, the elevation beamforming coefficients $\mathbf{w}(t)$ differ for different azimuth channels, as the reflector's secondary radiation patterns are non-separable [22]. Note that an antenna radiation pattern, $C(u, v)$ where $u = \sin\vartheta \cos\psi$ and $v = \sin\vartheta \sin\psi$, is separable if $C(u, v) = C(u)C(v)$, as is often the case for rectangular planar direct radiating antennas as a result of the separability of the current distribution. In some special cases, when simple elevation beamforming algorithms are applied, which do not aim at ambiguity suppression, the beamforming coefficients of a reflector system may, however, be azimuth-invariant. The range-azimuth diagram (cf. Part 1 [1]) for the case of two azimuth channels and concatenated swath SCORE is shown in Fig. 7. The data streams of all azimuth channels are acquired simultaneously but processed through different DBF units. In the figure, the range lines from different azimuth channels appear side-by-side and aligned in range; it should be kept in mind that this involves combining and aligning (synchronizing) output data streams from different FPGAs, a task which is not necessarily trivial.

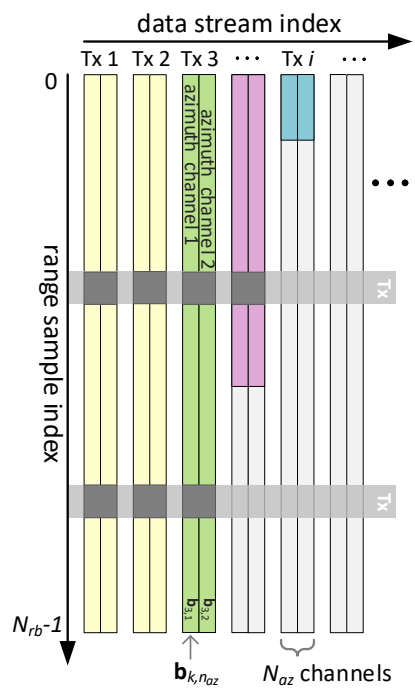

Figure 7: Range-azimuth data diagram for a concatenated swath SCORE with two azimuth channels; the range line data of each azimuth channel is processed by its own DBF unit.

At this point the notation is extended to account for multiple azimuth channels by adding a subscript, referring to the azimuth channel number, to all vectors and matrices. For example, the N_{rb}-element output beam is written as:

$$\mathbf{b}_{k,n_{az}} = \left[b_{k,n_{az}}[0], b_{k,n_{az}}[1], \ldots, b_{k,n_{az}}[N_{rb}-1] \right]^T \quad (5)$$

indicating the k-th output SCORE beam of the n_{az}-th azimuth channel, where $k = 1, \ldots, N_{beam}$ and $n_{az} = 1, \ldots, N_{az}$.

V. Beamforming Weights, Reflector Illumination and Secondary Beams

A topic mentioned in Part 1 of the tutorial [1] is the selection of the beamforming coefficients, i.e., the complex weights

applied on the data of the feed array elements to yield a desired antenna beam pattern. While it is understood that (in a reflector-feed antenna system) the activated feed element depends on the direction of the incoming wave, it has yet to be justified why a complex valued digital weight applied on the feed element's data should influence the resulting antenna radiation pattern. The aim here is to develop an understanding on how beamforming yields a certain desired radiation pattern.

Table I lists the reflector-feed antenna system's design parameters (reference SAR) used for the simulations in this section. The antenna system is capable of achieving nearly $17°$ of angular scan range (the look angle range corresponding to the $355\,\mathrm{km}$ swath is about $16°$). The antenna system has not been optimized for SAR performance in terms of ambiguity performance, but it is rather intended for highlighting various beamforming aspects. The actual reflector design is highly complicated (see, for example, the NISAR and BIOMASS reflector SAR missions [10], [23]) involving lots of engineering expertise taking into account issues such as the vibration of the reflector, blockage due to the satellite bus, and thermal design aspects. These are well beyond the scope of this tutorial paper, therefore the reader interested in SAR reflector design and instrument performance is referred to the available literature such as [24], [19], [25], [11], [26].

Table I: Parameters of the reflector and antenna feed array used for the reference SAR system and the beamforming examples.

parameter	value
reflector diameter, D	$15\,\mathrm{m}$
focal length	$13.5\,\mathrm{m}$
center frequency, f_0	$1.2575\,\mathrm{GHz}$
feed array, $N_{az} \times N_{el}$	3×22
feed element type	rectangular horn
element separation	$1.2\lambda \times 1.022\lambda$
feed size	$0.86\,\mathrm{m} \times 5.4\,\mathrm{m}$
feed tilt angle	$36.9°$
feed offset	$9\,\mathrm{m}$ (in elevation)

Instead of elaborating on the mathematical formalism, a descriptive approach in terms of the electromagnetic fields is favored here (a wealth of literature is available on beamforming algorithms such as [27], [28], [29], [16], [30].) For most of what follows, the feed elements are taken to be the source of electromagnetic radiation, thus considering a transmitting antenna which allows for a more straight forward explanation. Through Maxwell's equations it can be shown that reciprocity applies to electromagnetic theory within a linear and isotropic (but not necessarily homogeneous) medium [31]. One (of many) application of the reciprocity theorem is for antennas and antenna radiation patterns (provided the materials used for the antennas and feeds are linear): measuring (and describing) the pattern can conveniently be done either in the receiving or transmitting mode because they are identical [22].

The electric field strength distribution imposed by any single feed element is determined by the antenna type, e.g., horn, patch, and slotted waveguide. Its far field radiation pattern, i.e., the normalized electric field strength as a function of directional coordinates, is referred to as the *element pattern* following common antenna terminology. The total electric field strength excited by the complete feed array, known as the *primary radiation pattern*, is determined by: the element pattern, the array geometry (position of radiators), and the excitation. The latter depends on the amplitude and phase of the current at the input terminals of each feed antenna element. For identical radiators and assuming no coupling effects, the primary antenna pattern is the product of the element pattern and the *array factor*, where the latter is entirely determined by the feed geometry and the excitation.

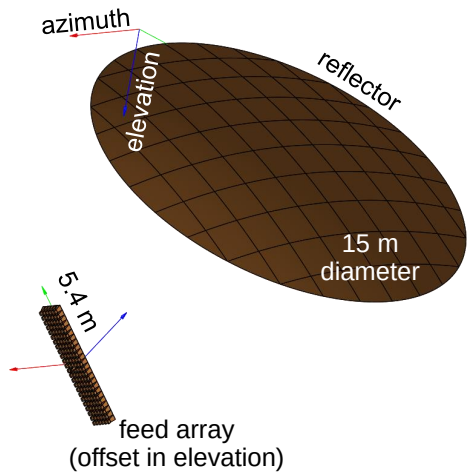

Figure 8: Reflector and feed array antenna geometry.

The feed array illuminates the reflector imposing a current distribution on its surface, which, in turn, results in a propagating electromagnetic wave [22]. The normalized field distribution in the far field as a function of directional coordinates is known as the *secondary radiation pattern*. An observer far away from the reflector measuring the field strength will experience the reflector surface as the source of electromagnetic radiation. Ignoring the contribution of the feed array's back radiation to the total field at the observer's position, this indicates that the feed array excitation could be removed without altering the secondary antenna pattern, as long as the currents imposed on the reflector surface remain the same. This explains why the power density on the reflector, referred to as the *illumination intensity*, is crucial for understanding the beamforming process.

The type of visualization used here to describe and analyze the reflector antenna system of Table I is shown in Fig. 9 and includes the following:

Feed Excitation:
The 24×3 feed array excitation (upper right) in elevation (row) and azimuth (column) as the normalized amplitude weights in decibels. Elements which are not activated appear in white.

Reflector Illumination:
Shown on the upper left represents the power density on the reflector surface normalized to the total power. The ordinate and abscissa refer to the elevation and azimuth (along-track) directions, respectively. Dashed contour lines indicate the $-3\,\mathrm{dB}$ and $-11\,\mathrm{dB}$ power density levels.

Secondary Radiation Pattern:
The resulting secondary gain pattern versus elevation angle is shown in (bold line) on the bottom together with the individual secondary gain patterns resulting from activating single feed rows (thin cyan lines). The maximum antenna pattern gain value is also included.

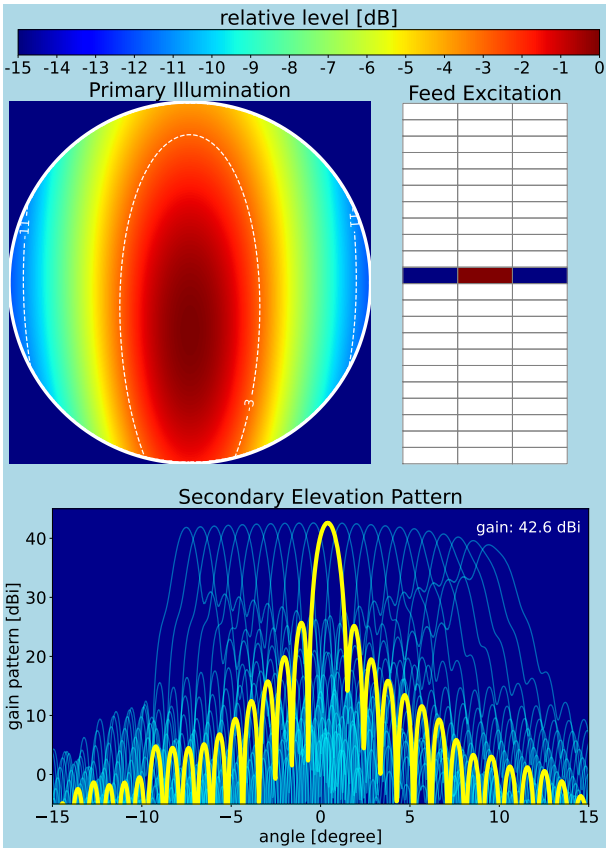

Figure 9: Reflector excitation, illumination and secondary radiation patterns. The center feed array row is activated.

Since the emphasis here is put on the elevation beamforming, the focus will be on the rows of the feed array which determine the secondary radiation pattern in elevation. The feed element columns are included for completeness and to yield a realistic representation (remember that reflector radiation patterns are non-separable). The three azimuth elements of each feed row are utilized to set the azimuth beam taper, which determines the azimuth radiation pattern cut for any specific elevation angle. Azimuth beamforming will be detailed in part 3 of the tutorial paper; it is thus suggested that at this point the center element of each row (center column of the feed array) is of most interest here.

A. Single Feed Row Activation

As detailed in part 1 the secondary beam direction (i.e., the direction of the main lobe of the secondary radiation pattern) of a reflector system is determined by the active feed element. Beam steering is thus achieved by activating different feed rows as shown in Fig. 10 (a) and (b).

Knowing that the reflector rim taper for optimum illumination efficiency is at $-10\,\mathrm{dB}$ to $-12\,\mathrm{dB}$ [22], it is seen that activating a single row causes an over-illumination in elevation (ordinate) direction. This is not a design flaw but rather a necessity to ensure smooth SCORE beam-to-beam transitions, cf. [1], [32]. As shown later, activating several rows provides a better illumination efficiency, thus yielding a higher gain (maximum value) of the secondary radiation patterns. The secondary gain patterns show a degradation when activating edge rows as seen in Fig. 10b which is due to the defocusing effect of the reflector geometry for large scan angles. The antenna pattern degradation is gradual, increasing with the distance of the feed element from the focal point of the parabolic reflector; this can be seen from the secondary radiation pattern plots (bottom) which also show the antenna patterns of all individual feed row excitations.

Comparing Fig. 9 to Fig. 10 (a) and (b) there is no significant difference in the illumination (amplitude) for the different activated rows. However, the position of the illumination maximum changes depending on the activated row and is *not* always fixed at the reflector's center. This is an indication that the mechanical feed elements' boresight direction is not pointed towards the reflector center and is understood as an unwanted side effect from using a planar feed array.

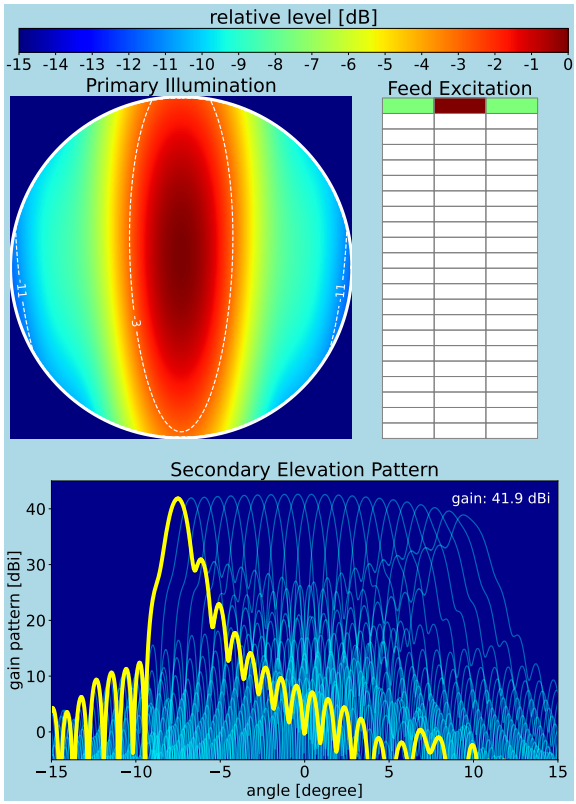

(a) first feed row active

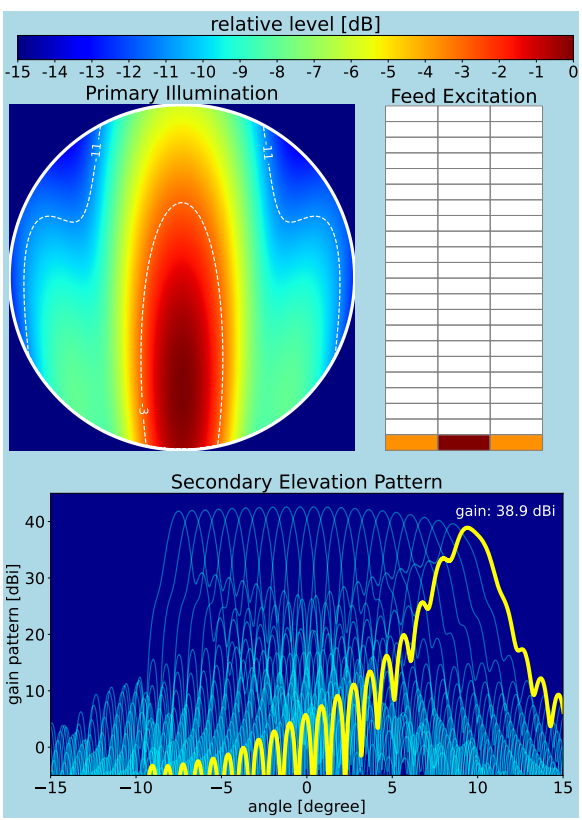

(b) last feed row active

Figure 10: Reflector excitation, illumination and secondary radiation patterns for the case that different rows of feed elements are activated.

B. Transmit Reflector Antenna Pattern

A somewhat unusual approach for a reflector-feed system is used on transmit to generate the wide secondary beam illuminating the complete swath. Here, all feed rows are activated to generate a narrow primary beam, which illuminates a small portion of the reflector, thus generating a wide secondary beam. Fig. 11 shows that this approach works as expected.

It is worth considering the effect of the widened illumination (large antenna beamwidth) on the radiation intensity, i.e., the power per unit solid angle measured in Watts per steradian. This is a crucial factor affecting the power density on the ground and through this the signal-to-noise ratio (SNR) of the echo signal at the receiver. The maximum radiation intensity as a function of the antenna's directivity, D_0, and radiated power, P_{rad}, is given by [22]:

$$p_\Omega = \frac{D_0}{P_{\text{rad}}/4\pi} \tag{6}$$

In a reflector-feed system with distributed (solid state) power generation the total transmitted, i.e., radiated, power depends on the number of active feed elements. To widen the secondary beam more elements are activated which increases the total radiated power P_{rad}. Since all elements are active on transmit [1] the maximum available power is radiated; for the underlying reflector system this increases the transmitted power by a factor of 22 or $13.4\,\text{dB}$. At the same time the increased secondary beamwidth causes a reduction in the antenna's directivity. This becomes evident from the following expression (cf. [22], [33])

$$D_0 = \frac{4\pi}{\oint_\Omega |C(\vartheta,\psi)|^2\,\mathrm{d}\Omega} \tag{7}$$

which relates the antenna directivity to the closed surface integral (for example a sphere enclosing the antenna) of the normalized secondary antenna radiation pattern $C(\vartheta,\psi)$. When increasing the beamwidth the contribution to the integral in the denominator of (7) increases, thus causing a reduced directivity. Similarly, the antenna gain is reduced, as it is proportional to the directivity for fixed antenna losses.

For a reflector antenna this is intuitively clear and is traced back to the definition of the antenna gain [22] as: *The ratio of the intensity, in a given direction, to the radiation intensity that would be obtained if the power accepted (input) by the antenna were radiated isotropically*. Adding active elements increases the radiated power and extends the beamwidth, but the additional available power is "distributed" into the wider mainlobe keeping, at least to a first approximation, the radiation intensity (within the increased mainlobe) constant! On the other hand, the effective radiation intensity generated by any feed element may be boosted by activating neighboring elements, which is due to the beam overlap, but basically unaffected by far-away elements. The antenna gain of the transmit configuration in Fig. 11 is approximately $32.5\,\text{dBi}$ which is considerably lower than that of single row activation, this confirms that an increased beamwidth is accompanied by a reduced antenna gain.

Despite the above two effects, i.e., increased power and reduced gain, more or less compensating each other, the

possibility of widening the coverage (swath) by adding feed elements is an advantage of reflector-based SAR over systems utilizing planar direct radiating antenna. In the latter, typically phase-spoiling excitation techniques [34], [35] are used to widen the antenna pattern, where, unlike a reflector-feed system, the total transmitted power P_{rad} remains constant and independent of the beamwidth, while the gain drops with increased beamwidth. This results in a *reduced* radiation intensity when illuminating a wider swath, which is a disadvantage of planar antenna SAR.

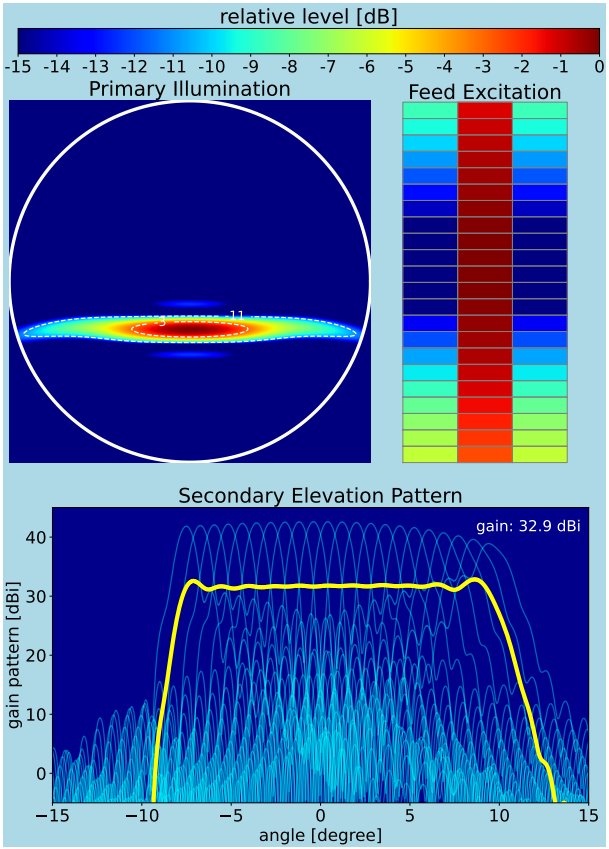

Figure 11: Reflector excitation, illumination and secondary radiation patterns for the transmit case where all feed elements are activated.

C. Optimum Beamformer

Next, an optimum beamformer is used, which maximizes the signal-to-noise ratio [27], [28], [29] — also known as Minimum Variance Distortionless Response (MVDR) beamformer. In the following, the number of active feed rows is limited to 4 and uncorrelated (receiver) noise is assumed, i.e., no interference or ambiguities. As seen from Fig. 12a the optimum beamformer steered to the boresight direction at 0° mainly excites two rows of the feed array with equal amplitudes. This generates a nearly ideal rim illumination of $-11\,\text{dB}$ resulting in a secondary antenna beam of slightly higher gain amounting to $43.5\,\text{dBi}$, than that of the individual single feed row used to form the beam of $42.6\,\text{dBi}$ (cf. Fig. 9).

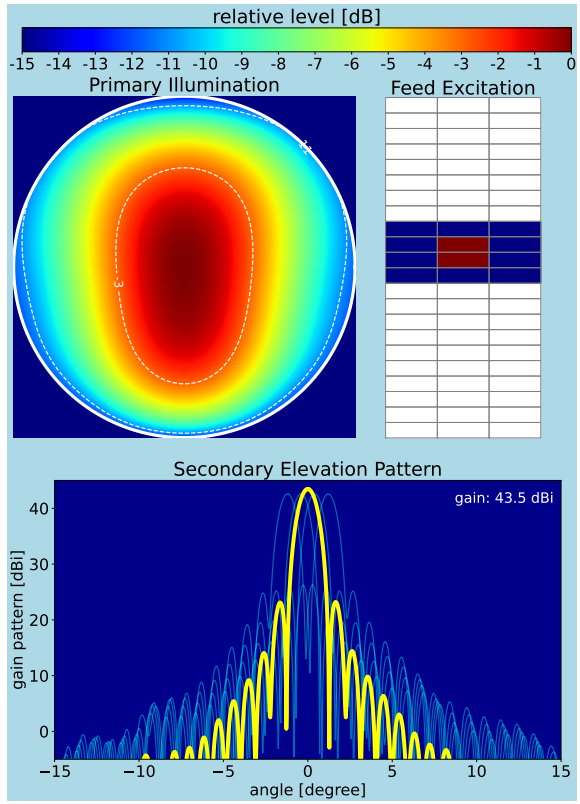

(a) optimum beam former @ 0°

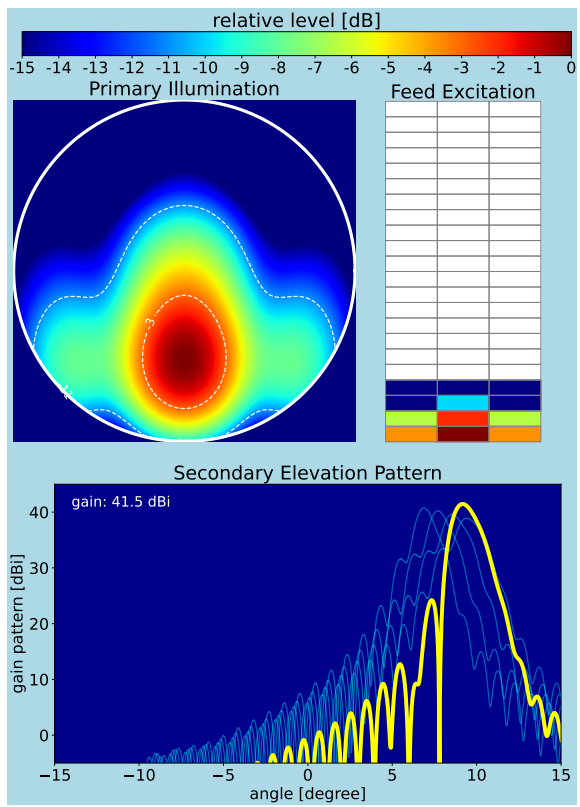

(b) optimum beam former @ 9.4°

Figure 12: Reflector excitation, illumination and secondary radiation patterns for an optimum beamformer designed to maximize the signal-to-noise ratio. The number of active feed rows has been limited to four.

Note that the secondary beam is pointing at the crossing point between two beam maxima; the "clean" secondary beam shape indicates a smooth SCORE beam-to-beam transition.

The defocusing, inherent to any reflector-feed system with scanning capabilities causes an antenna beam pattern degradation. Fig. 12b shows that beamforming can be used to mitigate this degradation to some extent. Comparing to the previous case, the feed excitation to steer the secondary beam towards $9.4°$ with respect to antenna boresight is "sophisticated" and more rows are active, a consequence of the beamforming compensating the defocusing effect. The reflector illumination shows a concentration on a smaller area which is shifted from the center; the former effect causes a gain reduction for the respective steering angle, while the latter is a consequence of the aforementioned feed element misalignment. Nevertheless, comparing Fig. 10b and Fig. 12b clearly shows that the optimum beamformer generates superior secondary radiation patterns in terms of sidelobe level and gain ($41.5\,\mathrm{dBi}$ versus $38.9\,\mathrm{dBi}$ gain).

D. Comparison of Different Beamformers

The performance of the beamforming is mainly determined by the shape of the secondary radiation pattern. Fig. 13 compares the previously introduced optimum beamformer to a sidelobe-constrained beamformer [16] both steered to an angle of $7.5°$ for a maximum of 7 active feed rows. The scale is extended to cover $0\,\mathrm{dB}$ to $-18\,\mathrm{dB}$ in order to emphasize the different weights and illumination. The optimum beamformer yields the narrowest radiation pattern beamwidth, while the sidelobe-constrained beamformer lowers the sidelobe level at the expense of a wider beamwidth and a slightly lower gain. In practice this is beneficial for SAR instruments, since the disturbance is not only made of thermal noise, but is also influenced by ambiguities; a sidelobe-constrained beamformer leads to slightly worse SNR, but a much higher ambiguity suppression.

Although the amplitudes of the feed array weights appear to be similar for the two cases, the beamformers utilize the active element excitation differently: the low-amplitude feed elements at $-18\,\mathrm{dB}$ have a minor effect on the reflector illumination for the optimum beamformer which shows a nearly ideal $-11\,\mathrm{dB}$ rim taper for maximum SNR; in the case of the sidelobe-constrained beamformer the low amplitude feed elements are used to mitigate the sidelobes caused by the higher amplitude feed elements, which manifests itself in the different reflector illumination.

One further factor to consider when comparing beamforming algorithms is the effect of the feed array's phase and amplitude errors on the resulting radiation pattern. These errors and other imperfections as well as calibration (covered for example in [36], [37], [38], [6], [39], [40], [41], [42], [43], [44]) are highly relevant but considered beyond the scope of this tutorial paper.

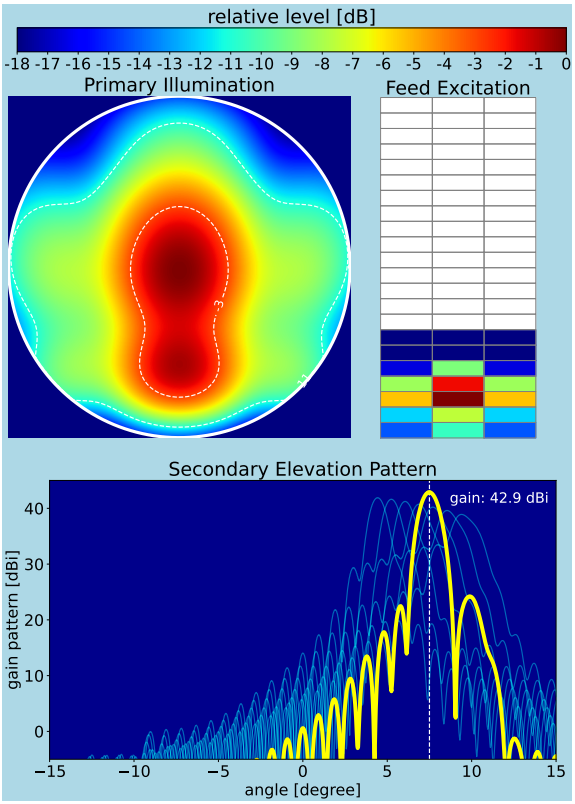

(a) optimum beam former

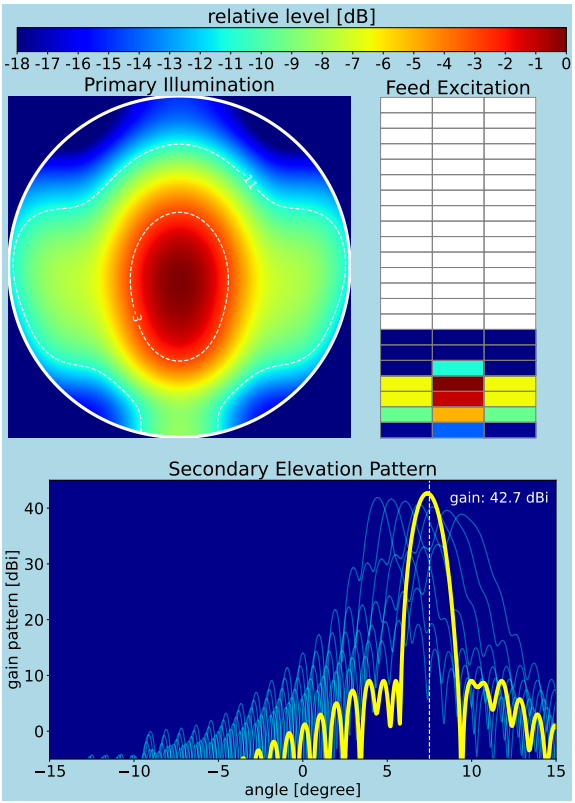

(b) sidelobe-constrained beamformer

Figure 13: Reflector excitation, illumination and secondary radiation patterns comparing an optimum and a sidelobe-constrained beamformer. The secondary antenna pattern is steered to $7.5°$.

The inherent usefulness of beamforming is shown by comparison to a unity, i.e., simple on-off, beamformer with two active feed rows shown in Fig. 14. The antenna pattern's peak of the latter may be slightly shifted with respect to the design value and yields an approximately $1\,\mathrm{dB}$ lower gain value with higher sidelobe level.

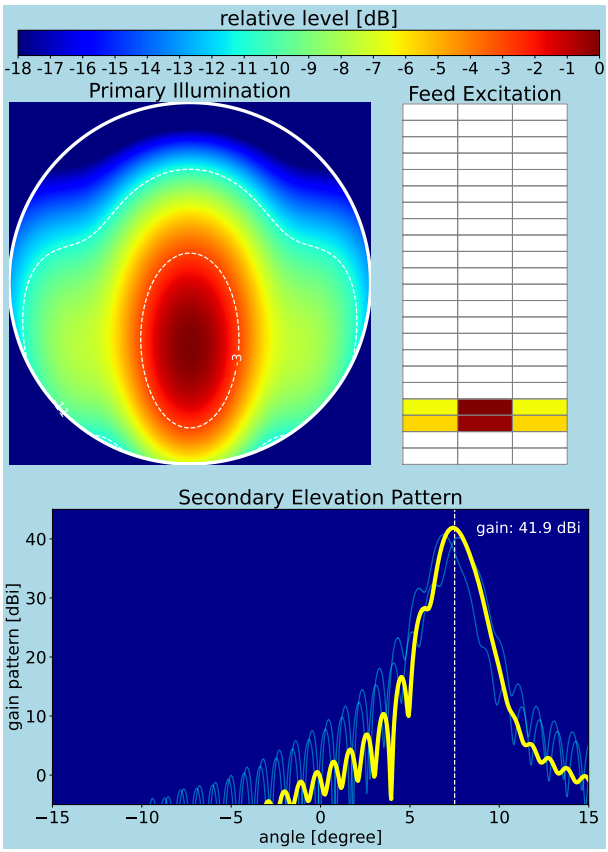

Figure 14: Reflector excitation, illumination and secondary radiation patterns for the case of a unity beamformer equally exciting two feed rows.

E. Multi-Beam Generation

The cases covered up to now were intended to foster the understanding of beam steering, the influence of the number of active elements and the different beamforming methods. However, the example radiation patterns given could all have been realized using an analog feed array (based on transmit/receive modules). The superiority of a digital feed array is that it allows generating multiple simultaneous beams which are independent from each other. From a DBF perspective, the excitation coefficients of multiple beams are generated by a simple complex valued superposition of the individual antenna beams' excitation coefficients.

In case of a receiving antenna system (remember that the reciprocity theorem mentioned earlier allows applying the same argumentation to a transmit or receive antenna) each beam generates its own data stream; in terms of hardware schematic either DBF unit configuration of Fig. 4 (b) or (c) may be utilized.

Fig. 15a shows the feed excitation resulting in three (simultaneous) antenna beams which are steered to the center of the imaged sub-swaths of the reference SAR. Each beam activates 4 feed rows and the large angular separation between the secondary antenna beams yields non-overlapping (disjunctive) active feed rows. It is emphasized that each secondary antenna beam can be understood as generated by its own independent antenna. Thus, although the secondary antenna patterns are plotted on a common abscissa, they do *not* represent a joint radiation pattern of the three antenna beams. From the beamforming perspective each secondary radiation pattern is associated to its own data stream and distinct excitation coefficient (the index k is used in (2) to indicate the beam number of the output data stream $\mathbf{b}_k$). This explains the high gain of each beam, in the order of $43.5\,\mathrm{dBi}$. The ability to generate multiple beams while maintaining a high gain for each antenna beam is considered a main advantage of digital beamforming systems.

The reflector illumination shows the typical interference pattern known to occur from the coherent superposition of multiple radiation sources. It is worth investigating whether (and how) this interference pattern affects the individual radiation beam patterns. For this, consider a feed array excitation imposing a $-11\,\mathrm{dB}$ rim illumination resulting in a single output beam. Imagine an observer in the far field measuring the electric field strength at the maximum of the secondary radiation pattern.

Now, in a second step, the excitation weights are modified to add a second beam causing the interference patterns to appear on the reflector surface. The observer will not measure any change in the electric field strength, provided that the angular separation of the two beams is sufficiently large. This effect can be traced back the superposition principle of electromagnetic waves in linear medium and shows that the focusing property of the reflector geometry maintains the angular orthogonality of the beams generated by spatially separated feed elements. It is worth mentioning that the primary illumination pattern shown Fig. 15a corresponds to *a single* secondary radiation pattern with *three main lobes*; although, in this sense, the representation could be misleading it is considered beneficial for understanding the functionality of the reflector antenna system.

To elaborate on the multi-beam issue, Fig. 15b shows a DBF configuration for two closely spaced reflector beams, each generated by 4 active feed rows. Clearly, there is an overlap between the feed elements of the two beams, however, the gain of the individual beam is maintained. Because of the active feed element overlap a concatenated swath DBF topology, cf. Fig. 6, is the suitable choice. The reflector illumination in Fig. 15b shows two distinct active areas. These are due to the coherent interference of the excitation sources and should *not* be mistaken to correspond to the two beams. Note that the rim illumination of each active area is well below $-20\,\mathrm{dB}$, which cannot yield the high gain of the secondary beams. Illuminating different areas of a reflector generates overlapping secondary antenna beams and has been suggested for along-track interferometry using a single reflector antenna [45], [46].

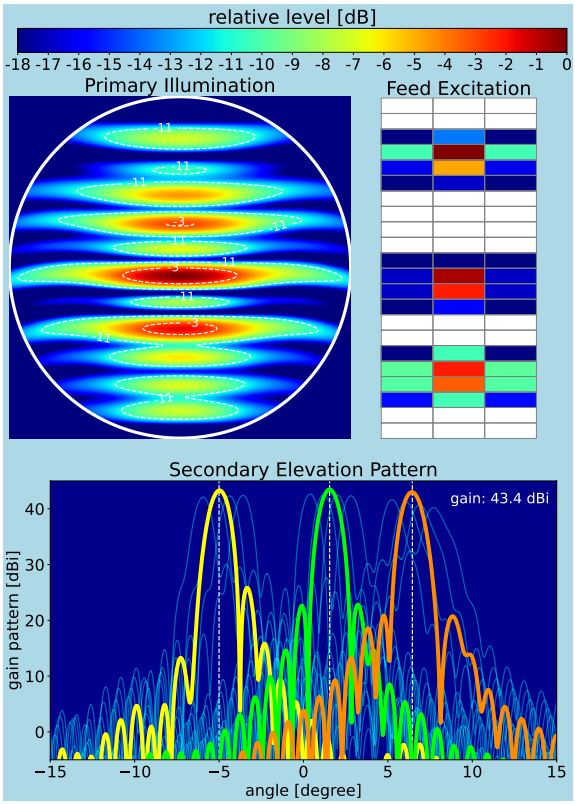

(a) optimum beam former with two SCORE beams

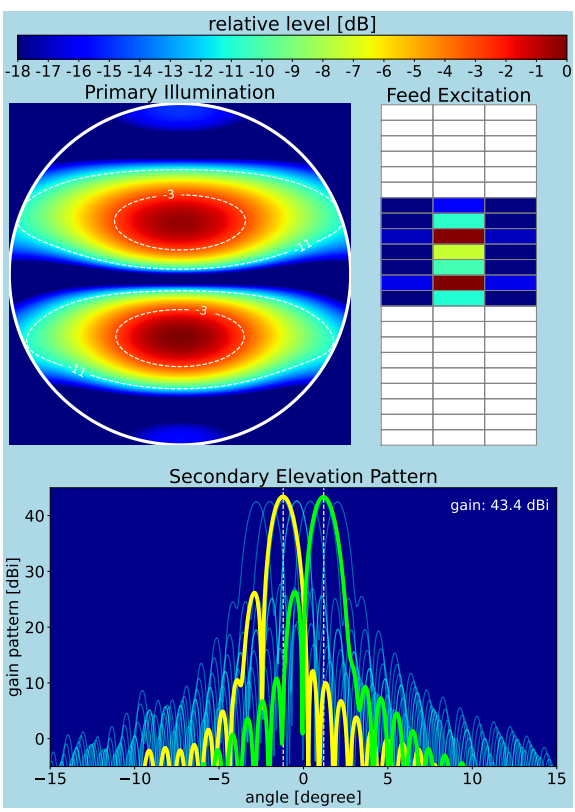

(b) optimum beam former with five SCORE beams

Figure 15: Reflector excitation, illumination and secondary radiation patterns for multi-beam SCORE operation.

VI. Blind Ranges

The second issue mentioned in section II were imaging gaps (blind ranges) due to the transmit events. These are detailed in this section and a closed form expression relating the blockage to the resulting image gap is derived. Blind ranges occur when there is a transmit event during the time an echo should be received, which is unavoidable when the swath is large such that $T_{echo} > T_{\text{pri}}$. The impact of the blind ranges are gaps in the processed SAR image [47], [48], [49], which, for a uniform PRF, appear at fixed ground range positions in the swath, as illustrated schematically in Fig. 16. The gaps occur periodically at integer multiples of the PRI, i.e., at time delays $n \cdot T_{\text{pri}}$ corresponding to the slant ranges $n \cdot cT_{\text{pri}}/2$ where n is an integer.

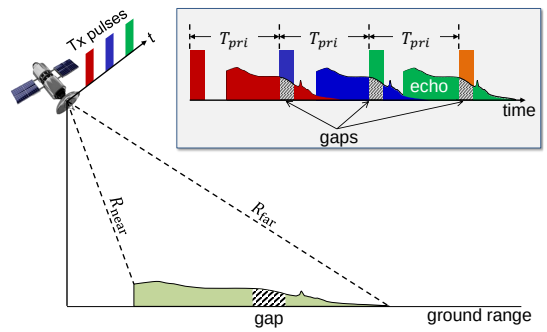

Figure 16: Schematic representation of transmit instances and the received echoes, causing gaps and range ambiguities.

The time at which the SAR receiver is turned off during the transmit events is known as the blockage time and is denoted by τ_b. Due to the guard time — the time needed for the limiter diode in the receive path to recover — the blockage duration is typically longer than the transmit pulse $\tau_b \geq \tau_p$ as shown in Fig. 17. It should be noted that any transmit event will block all N_{el} input data streams and for all output beams; thus for each transmit event $\tau_b \cdot f_s$ samples will be lost for each channel, which is in the order of a few thousand samples. Depending on the PRF and the swath width, each range line may be interrupted several times due to the multiple transmit events within the echo time T_{echo}. The average number of gaps within the swath is equal to $N_{beam} - 1$, where N_{beam} has been introduced earlier in (1) and represents the average number of beams.

Parameter Values: The reference system images a swath of $355\,\text{km}$ through $N_{beam} = 3$ simultaneous SCORE beams. The diamond diagram in Fig. 1 shows that the swath is interrupted by $N_{beam} - 1 = 2$ gaps. The blockage time τ_b is determined by the pulse duration $\tau_p = 34\,\mu\text{s}$ plus the guard time of $4\,\mu\text{s}$.

Nadir echo returns may also cause blind ranges, for which they need to be considered [50]. For reflector-based SAR, however, the nadir return may be sufficiently attenuated by the Rx/Tx antenna pattern. Furthermore, novel techniques for the removal of the nadir echo within post-processing based on the alternation of the transmitted waveform are suggested in

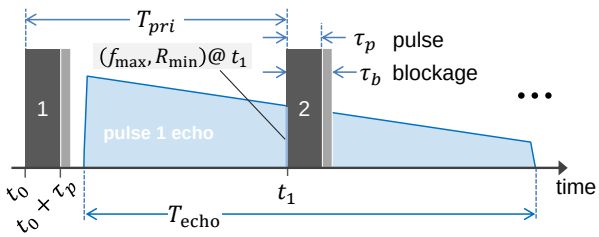

Figure 17: The transmit pulse (duration τ_p) and the associated guard time cause a blockage of the return echo during τ_b seconds. To determine the width of the resulting imaging gap it is necessary to consider the instantaneous frequencies of the return echo which are blocked for each range.

[51], [52]; as an additional benefit these techniques allow for relaxing the PRF constraint.

A. Imaging Gap Extent

The expression for the imaging gap extent is derived taking the transmitted signal time-frequency dependency into account in order to quantitatively assess the impact on the imaging performance.

Consider a stationary radar, which, without restriction of generality, is transmitting an up chirp, pulse 1, of duration τ_p. Take a reference sphere centered at the antenna just large enough to contain the complete antenna structure. Let t_0 and $t_0 + \tau_p$ mark the time instances where the leading and lagging "edge" of an electromagnetic wave generated by the transmitted pulse pass the reference sphere. The corresponding instantaneous frequencies are f_{min} and f_{max} respectively.

After a time delay of ΔT seconds, the distance r between the reference sphere and the leading pulse edge will be $c \cdot \Delta T$. The echo reflected from a point scatter at range r will intersect the reference sphere at times

$$t = t_0 + 2\Delta T = t_0 + \frac{2r}{c} \quad \text{and} \quad t = t_0 + \tau_p + \frac{2r}{c} \tag{8}$$

for the leading and lagging pulse edge, respectively. The term $(2r)/c$ in the above expression, well known from the radar delay equation, may be rearranged to read $r/(c/2)$. It can be deduced that to an observer the echo appears to be traveling at $c/2$ which is *half* the speed of light.

Now consider a second transmission event occurring at time t_1 which is blocking the receiver for τ_b seconds. The blocked slant range limits are given by the *minimum* slant range R_{min} of the *lagging* pulse edge at t_1 and the *maximum* slant range R_{max} of the *leading* pulse edge at $t_1 + \tau_b$. With (8) the ranges are determined from the following equations:

$$(t_0 + \tau_p) + \frac{2R_{min}}{c} = t_1 \quad \text{and} \quad t_0 + \frac{2R_{max}}{c} = t_1 + \tau_b \tag{9}$$

The slant range extent of the gap is obtained by solving for R_{min} and R_{max} and forming the difference:

$$\chi_r = R_{max} - R_{min} = \frac{c}{2}(\tau_b + \tau_p) \tag{10}$$

The above expression gives the total slant range extent of the blockage without considering which frequencies are blocked at which ranges. The correspondence between range and frequency is also addressed in the context of dispersive beamforming of tutorial part 1 [1]. It is crucial to understand the range-frequency behavior of the blockage as detailed next.

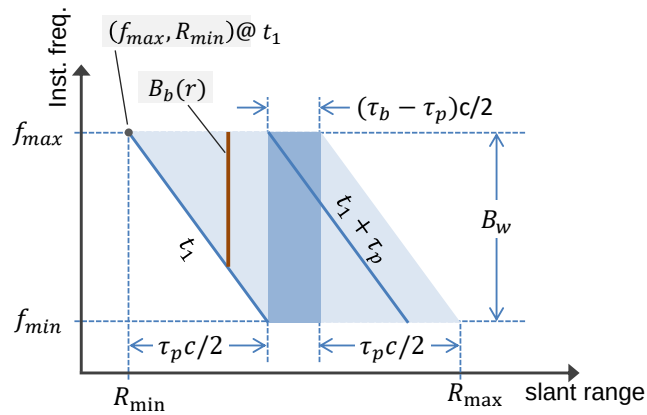

Figure 18: Frequency-range diagram for an up chirp showing the gap extent. The dark-shaded rectangle indicates full blockage, while the two light shaded triangles represent the partial bandwidth blockage. Horizontal and vertical lines represent lines of constant frequency and slant range, respectively.

The blockage start time is t_1, at which the lagging edge of the pulse will be at range R_{min}, for which the instantaneous frequency f_{max} will be blocked. This point is indicated by (f_{max}, R_{min}) in Fig. 18 illustrating the blocked instantaneous frequencies versus slant range; here, horizontal and vertical lines represent lines of constant frequency and slant range, respectively. The linear time-frequency relation of the chirp manifests itself in a linear range-frequency blockage relation. The line marked t_1 in the figure represents a range-frequency notch between R_{min} and $R_{min} + \tau_p c/2$ for the frequencies f_{max} to f_{min}. Similarly, the instantaneous frequencies and ranges blocked at time instance $t_1 + \tau_p$ are indicated in the figure. The range of frequencies blocked for any range r is indicated by the vertical line and bandwidth $B_b(r)$.

From the above it is concluded that the slant range extent of the gap, i.e., the width of the strip in the range compressed image which is lost due to the transmit event is divided into two regions:

- A full blockage occurring at ranges for which there is a total loss of received echo pulse power, indicated by the dark shaded rectangle in Fig. 18, and
- A partial blockage for those ranges at which part of the pulse power is received, as indicated by the light shaded region (two triangles) in Fig. 18.

The extent of the gap is then defined in terms of the blockage bandwidth $B_b(r)$, i.e., the range of frequencies which *cannot* be received due to the transmit event. The expression for the blockage in terms of the slant range for each of the two regions is:

$$\chi_r\big|_{B_b(r)<B_w} = \tau_p c \qquad \text{partial blockage} \tag{11}$$

$$\chi_r\big|_{B_b(r)=B_w} = \frac{(\tau_b - \tau_p)c}{2} \qquad \text{full blockage} \tag{12}$$

where the ground range extent χ_g [53] can be readily obtained through $\chi_g = \chi_r / \sin \eta_i$ with η_i being the incidence angle.

The above result is interesting because it shows that the full-bandwidth blockage causing a complete loss of signal energy and an imaging gap is proportional to the guard time interval $(\tau_b - \tau_p)/2$, which is small compared to the pulse duration. This is shown in Fig. 19 for the reference system, where the full bandwidth gap is less than $1\,\mathrm{km}$ in ground range. The major contribution to the blockage is partial, where only part of the echo signal power is retrieved leading to a worsening of the range resolution because of the blocked frequencies; further, the reduced bandwidth needs to be taken into account in the range focusing to avoid an SNR degradation.

Parameter Values: As mentioned previously, the reference system images a $355\,\mathrm{km}$ swath interrupted by 2 gaps. In slant range, the width of the total and partial bandwidth gaps is constant at $600\,\mathrm{m}$ and $10.1\,\mathrm{km}$, respectively. The ground range extent of the gaps depend on the incidence angle as listed in the following table.

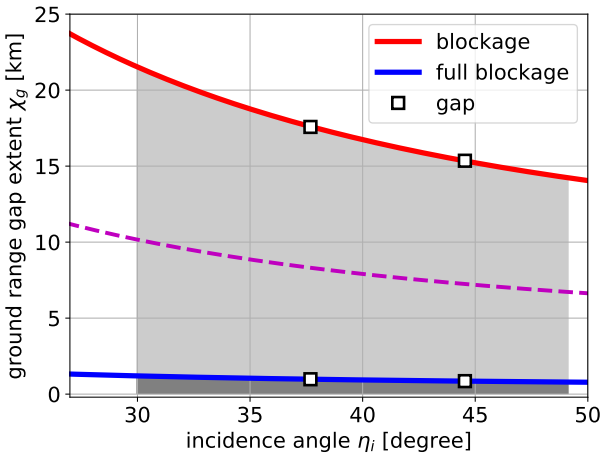

Figure 19: Ground range extent of image gap χ_g versus incidence angle. The lower curve shows the full-bandwidth gap while the upper curve is the total (partial + full) gap. The dashed curve gives the gap extent corresponding to half the range bandwidth. The parameters are those of the reference system operating at a pulse duty cycle of $6\,\%$ and a blockage time of $\tau_b = 38\,\mu\mathrm{s}$; the positions of the two imaging gaps are indicated by the squares.

incidence angle	gap (full)	gap (full+partial)	50% blockage partial
37.7°	980 m	17.6 km	8.3 km
44.5°	855 m	15.4 km	7.2 km

Table II: Angular position and ground extent of imaging gaps of different types assuming spherical Earth geometry.

VII. Data Streams and Memory Management

Up to now it has been detailed how multiple echoes are collected simultaneously through multiple SCORE beams and azimuth channels. In the following, the correspondence between the samples of the echo lines and the (buffer) memory is reviewed, as it is crucial for understanding the on-board data processing.

Let the first pulse Tx 1 be transmitted at time t_0; the near range echo will arrive after $2R_{near}/c$ seconds and last for T_{echo} seconds. During this time, the signal from a changing subset of the feed elements is sampled, weighted and summed up. The resulting N_{rb}-element vector of azimuth channel n_{az} (known as *range line*) is $\mathbf{b}_{1,n_{az}}$. The data stream is written into a memory block sufficient to store $2N_{rb}$ real-valued samples (the factor 2 accounts for the complex valued echo data, thus one real and one imaginary value is stored per sample) where each sample occupies M_{bit} bits of memory.

The number of samples N_{rb} as given by (4) in Part 1 of the tutorial is for continuous data acquisition during the complete echo time T_{echo}. In this case the blocked data samples still occupy memory space; this is necessary when data samples are later to be recovered through an on-board interpolation process as is the case in Staggered SAR operation mode detailed in Part 3 of the tutorial to be published in a later issue of the GRS Magazine. Otherwise, no memory allocation for the samples lost during the blockage times is necessary and the number of stored samples per range line may be reduced. Taking into account the previously mentioned blockage times, the (reduced) number of samples per range line becomes:

$$N_{rb} = T_{echo} f_s - \tau_b (N_{beam} - 1) f_s \tag{13}$$

The echo of Tx 1 is received and processed by all N_{az} azimuth channels simultaneously, each azimuth channel n_{az} produces the output $\mathbf{b}_{1,n_{az}}$. In total, for each echo N_{az} data streams are written simultaneously into memory.

At time $t_0 + T_{\text{pri}}$ the second Tx 2 pulse is transmitted; its echo arrives *before* the end of the first echo, thus

$$(t_0 + T_{\text{pri}}) + \frac{2R_{near}}{c} < t_0 + \frac{2R_{near}}{c} + T_{echo} \tag{14}$$

which indicates that there is an overlap time during which two echoes $\mathbf{b}_1$ and $\mathbf{b}_2$ from different range positions are received simultaneously. Since the reflector focuses these echoes on different sets of elements, they can be separated by DBF to produce separate, i.e., independent, data streams. The above expression is equivalent to $T_{\text{pri}} < T_{echo}$ which has already been stated in section II as a particularity of ultra-wide swath imaging. As before, the data streams $\mathbf{b}_{2,n_{az}}$ with $n_{az} = 1 \cdots N_{az}$ are assigned to N_{az} memory blocks each of $2N_{rb} \cdot M_{bit}$ bits.

Parameter Values: In conventional SAR systems (last generation) the number of ADC bits M_{bit} per (real) sample is typically $8\,\mathrm{bit}$. State-of-the-art SAR instrument use a larger number of bits, in the order of $8\,\mathrm{bit}$ per sample, due to the increased system dynamic range. In DBF SAR this is further increased for the internal SCORE beamforming operations such that M_{bit} becomes $16\,\mathrm{bit}$ to $20\,\mathrm{bit}$.

As the echo signals from subsequent transmit pulses Tx i are received, more SCORE beams are added, up to a maximum of N_{beam} data streams. When the echo of the first transmit pulse reaches the far swath limit, the SCORE beam will be pointing to far range R_{far} and the number of SCORE beams is reduced by one, until a new near range R_{near} echo arrives requiring re-assigning the data stream $\mathbf{b}_{1,n_{az}}$ to that echo.

A. Data Rate and Azimuth Oversampling

The digital system architecture and design is driven by the high data rates of DBF SAR instruments. In the following, expressions for the data rate after SCORE, i.e., applied on the $\mathbf{b}_{k,n_{az}}$ data given in (5), are derived.

Referring to Fig. 20, any arbitrary PRI time interval T_{pri} may be divided into three segments:

1) during $T_1 = T_{echo} - (N_{beam} - 1)T_{\text{pri}}$ seconds, the data from N_{beam} beams are acquired
2) during $T_2 = N_{beam}T_{\text{pri}} - \tau_b - T_{echo}$ seconds, $N_{beam} - 1$ data streams are acquired
3) during the remaining τ_b seconds no data are acquired (blockage)

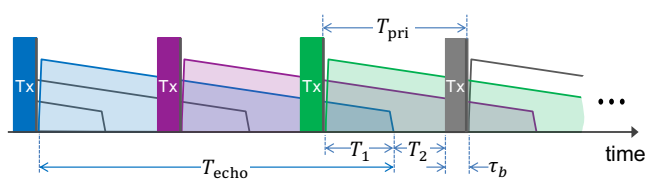

Figure 20: Timing of (overlapping) ground return echo signals from successive (color-coded) transmitted pulses for $N_{beam} = 3$ simultaneous SCORE beams. The average data rate is computed considering the interval T_{pri} which is divided into three segments T_1, T_2, and τ_b.

Summing the samples of each interval, dividing by T_{pri} and collecting terms yields an average of:

$$\frac{2f_s}{T_{\text{pri}}}T_{echo} - \frac{2f_s}{T_{\text{pri}}}\tau_b(N_{beam} - 1) \tag{15}$$

(real) samples per second per azimuth channel. The first term accounts for the sampling of the echo signal (note that $T_{echo}/T_{\text{pri}} > 1$ in a multi-beam system), while the second term reduces the number of sample in proportion to the blockage duration.

Quantizing at M_{bit} bit/sample and considering all N_{az} azimuth channels, the total average data rate is obtained from (15) after substituting $f_{\text{prf}} = 1/T_{\text{pri}}$ to be:

$$D_r = 2f_s\left[T_{echo} - \tau_b(N_{beam} - 1)\right]\left[f_{\text{prf}}N_{az}\right]M_{bit} \tag{16}$$

in $\text{bit}\,\text{s}^{-1}$. Three terms appear in the above expression which are linked to the SAR instrument performance:

i) The (fast time) sampling rate f_s, which is proportional to the chirp bandwidth B_w (a large bandwidth leads to a fine range resolution) through $f_s = \gamma_r B_w$, where γ_r is the range oversampling.
ii) the echo time T_{echo} proportional to the imaged swath width as given by (2) in part 1 [1]
iii) the effective azimuth sampling $f_{\text{prf}}N_{az}$ determined by the azimuth resolution as explained below.

The last point deserves further explanation: A significant performance parameter is the azimuth resolution of the SAR image δ_{az}, which is measured in meters and given by [54]:

$$\delta_{az} = \frac{V_g}{B_{pD}} \tag{17}$$

with V_g the ground (or beam) velocity [55], [56] and B_{pD} the processed Doppler bandwidth. Clearly a good azimuth resolution can be achieved for a large Doppler bandwidth which, in turn, requires a wide azimuth antenna beamwidth, an adequate instrument design, and suitable processing algorithms [57], [7], [58], [59], [60], [61], [62]. On the other hand, the echo signal effective azimuth sampling rate, given by $f_{\text{prf}}N_{az}$, must be larger than the Doppler bandwidth as proven by the Shannon-Nyquist sampling theorem [63] since otherwise azimuth ambiguities would occur. A trade-off between the azimuth and range ambiguities must be also considered when selecting the oversampling ratio [7]

Putting the sampling rate in relation to the Doppler bandwidth allows defining the azimuth oversampling factor as:

$$\gamma_{az} = \frac{f_{\text{prf}}N_{az}}{B_{pD}} \geq 1 \tag{18}$$

which gives a quantitative measure of the system resources overhead in terms of the azimuth sampling to performance parameter (resolution) ratio.

Nyquist-Shannon sampling also applies in range to the received echo as detailed in Part 1 of the tutorial [1]. A high range oversampling, $\gamma_r > 1$ may be of interest, if the RF system bandwidth (bandpass filter at the receiver front-end) is larger than the signal bandwidth as, in this case, it allows suppressing the noise outside the signal bandwidth. This, however, is at the cost of a higher internal data rate [64], [65].

Parameter Values: Azimuth oversampling is required, because the azimuth signal is not band limited due to the non-rectangular antenna pattern shape. For a stripmap SAR the azimuth oversampling γ_{az} is in the order of 1.2 to 1.4. Range oversampling is typically smaller and in the order of $\gamma_r \approx 1.1$.

The expression in (16) is a general approximation for the data rate valid for a multi-azimuth multi-beam system; it is also applicable for a basic SCORE system in which case $N_{beam} = 1$ and the echo time T_{echo} is that of a single swath return.

Parameter Values: Take the parameters of the reference system and a sampling frequency of $f_s = 85\,\text{MHz}$. Then the data rate for one azimuth channel is determined from (16) to be $D_r \approx 870\,\text{MByte/s}$ where $M_{bit} = 16\,\text{bit}$. Including the data samples during the blockage time results in a slightly higher data rate of $D_r \approx 916\,\text{MByte/s}$.

VIII. Conclusion

This paper provides a tutorial-type introduction to the basic DBF imaging modes of SAR utilizing a reflector antenna in conjunction with a digital feed array. Part 1 has shown the instrument architecture of a multi-channel SAR system and how it may be utilized for digital beamforming. Specifically, basic single-beam dispersive SCORE has been introduced and the associated functional digital instrument architecture explained.

Part 2 addresses ultra-wide swath imaging. The digital beamforming hardware enables multiple simultaneous SCORE beams, where each beam can be thought of as imaging an additional sub-swath and by this extending the total imaged swath. Two variants of this operation technique, partitioned swath and concatenated swath SCORE, are detailed. SCORE is performed on-board and is transparent to the subsequent SAR processing (range and azimuth compression), which may be implemented the same as for stripmap imaging mode. Well-known processing techniques developed for conventional SAR are therefore directly applicable. Section V fosters the understanding of the reflector-based beamforming process (with emphasis on the elevation direction) underlying the functional instrument implementation. Examples for the feed array excitation coefficients, the reflector illumination, and the resulting secondary radiation patterns are given and explained including the case of multiple beams. Multi-beam imaging allows for ultra-wide swath imaging but it comes at the expense of gaps between the sub-swaths. The blockage effect is analyzed in detail showing that most of the image gaps due to the transmit events are partial, thus allowing for the retrieval of some echo signal. Last but not least, after introducing the notation for multiple azimuth channels, the aspect of data streams, and the associated data rates are addressed. This is significant because the high data rate poses a challenge to the digital instrument design.

The above mentioned imaging gaps may be removed through a special operation technique, which is the main topic of tutorial Part 3 dealing with staggered SAR [66], [67]. This is a highly advanced technique where the pulse repetition interval is changed on a pulse-to-pulse basis according to a pre-determined sequence. This also affects the SAR azimuth and range performance and requires dedicated mitigation techniques.

References

[1] M. Younis, F. Q. de Almeida, M. Villano, S. Huber, G. Krieger, and A. Moreira, "Digital beamforming for spaceborne reflector-based synthetic aperture radar. Part 1: Basic imaging modes," *IEEE Geoscience and Remote Sensing Magazine*, Sept. 2021. [Online]. Available: https://www.nxtbook.com/nxtbooks/ieee/geoscience_september2021

[2] I. G. Cumming and F. H. Wong, *Digital Processing of Synthetic Aperture Radar Data: Algorithms And Implementation*. Artech House, 2005.

[3] F. D. Zan and A. M. Guarnieri, "TOPSAR: Terrain observation by progressive scans," *IEEE Transactions on Geoscience and Remote Sensing*, vol. 44, no. 9, pp. 2352–2360, Sept. 2006.

[4] M. Younis, "Digital beam-forming for high resolution wide swath real and synthetic aperture radar," Ph.D. dissertation, Institut für Höchstfrequenztechnik und Elektronik, Universität Karlsruhe, July 2004.

[5] N. Gebert, "Multi-channel azimuth processing for high-resolution wide-swath SAR imaging," Ph.D. dissertation, German Aerospace Center (DLR), Aug. 2009.

[6] S. Huber, "Spaceborne SAR systems with digital beamforming and reflector antenna," Ph.D. dissertation, Deutsches Zentrum für Luft- und Raumfahrt: Forschungsbericht, Sept. 2014.

[7] G. Krieger, N. Gebert, M. Younis, F. Bordoni, A. Patyuchenko, and A. Moreira, "Advanced concepts for ultra-wide swath SAR imaging," in *Proc. European Conference on Synthetic Aperture Radar EUSAR'08*, Friedrichshafen, Germany, June 2008.

[8] M. Younis, F. Bordoni, N. Gebert, and G. Krieger, "Smart multi-aperture radar techniques for spaceborne remote sensing," in *Proc. Int. Geoscience and Remote Sensing Symposium IGARSS'08*, Boston, MA, USA., July 2008.

[9] M. Younis, A. Patyuchenko, S. Huber, G. Krieger, and A. Moreira, "A concept for high performance reflector-based synthetic aperture radar," in *Proc. Int. Geoscience and Remote Sensing Symposium IGARSS'2010*, Honolulu, Hawaii, July 2010.

[10] Jet Propulsion Laboratory (JPL). (2022, July) The NASA ISRO SAR mission NISAR: Quick facts. [Online]. Available: https://www.mbie.govt.nz/science-and-technology/science-and-innovation/funding-information-and-opportunities/investment-funds/catalyst-fund/catalyst-strategic-new-zealand-german-aerospace-centre-joint-research-programme/

[11] P. Rosen, S. Hensley, S. Shaffer, W. Edelstein, Y. Kim, R. Kumar, T. Misra, R. Bhan, and R. Sagi, "The NASA-ISRO SAR (NISAR) mission dual-band radar instrument preliminary design," in *Proc. Int. Geoscience and Remote Sensing Symposium IGARSS'2017*, Fort Worth, USA, July 2017.

[12] A. Freeman, G. Krieger, P. Rosen, M. Younis, W. Johnson, S. Huber, R. Jordan, and A. Moreira, "SweepSAR: Beam-forming on receive using a reflector-phased array feed combination for spaceborne SAR," in *Proceedings IEEE Radar Conference (RadarCon'09)*, Pasadena, U.S.A., May 2009.

[13] Japan Aerospace Exploration Agency (JAXA). (2021, Apr.) Advanced Land Observing Satellite-4 (ALOS-4). [Online]. Available: https://global.jaxa.jp/projects/sat/alos4/

[14] M. Davidson, N. Gebert, and L. Giulicchi, "ROSE-L — The L-band SAR Mission for Copernicus," in *Proc. European Conference on Synthetic Aperture Radar (EUSAR)*, virtual, Mar. 2021.

[15] M. Villano, G. Krieger, and A. Moreira, "Staggered SAR: High-resolution wide-swath imaging by continuous PRI variation," *IEEE Transactions on Geoscience and Remote Sensing*, vol. 52, no. 7, pp. 4462–4479, July 2014.

[16] F. Q. de Almeida, T. Rommel, M. Younis, G. Krieger, and A. Moreira, "Multichannel staggered SAR: System concepts with reflector and planar antennas," *IEEE Transactions on Aerospace and Electronic Systems*, vol. 55, no. 2, pp. 877–902, Apr. 2019.

[17] G. Krieger, I. Hajnsek, K. Papathanassiou, M. Eineder, M. Younis, F. De Zan, P. Prats, S. Huber, M. Werner, H. Fiedler, A. Freeman, P. Rosen, S. Hensley, W. Johnson, L. Veilleux, B. Grafmüller, R. Werninghaus, R. Bamler, and A. Moreira, "The Tandem-L mission proposal: Monitoring Earth's dynamics with high resolution SAR interferometry," in *Proceedings of the IEEE Radar Conference*, Pasadena, U.S.A., May 2009.

[18] A. Moreira, G. Krieger, I. Hajnsek, K. Papathanassiou, M. Younis, P. López-Dekker, S. Huber, M. Villano, M. Pardini, M. Eineder, F. D. Zan, and A. Parizzi, "Tandem-L: A highly innovative bistatic SAR mission for global observation of dynamic processes on the earth's surface," *IEEE Geoscience and Remote Sensing Magazine*, vol. 3, no. 2, pp. 8–23, June 2015.

[19] S. Huber, F. Q. de Almeida, M. Villano, M. Younis, G. Krieger, and A. Moreira, "Tandem-L: A technical perspective on future spaceborne SAR sensors for earth observation," *IEEE Transactions on Geoscience and Remote Sensing*, vol. 56, no. 8, pp. 4792–4807, Aug. 2018.

[20] M. Younis, F. Q. de Almeida, F. Bordoni, P. López-Dekker, and G. Krieger, "Digital beamforming techniques for multi-channel synthetic aperture radar," in *Proc. Int. Geoscience and Remote Sensing Symposium IGARSS'2016*, Beijing, China, July 2016.

[21] F. Almeida, M. Younis, G. Krieger, and A. Moreira, "Multichannel staggered SAR azimuth processing," *IEEE Transactions on Geoscience and Remote Sensing*, vol. 56, no. 5, pp. 2772–2788, May 2018.

[22] C. A. Balanis, *Antenna Theory: Analysis and Design*, 4th ed. Chichester New York: John Wiley & Sons, 2016.

[23] European Space Agency (ESA). (2022, July) BIOMASS ESA's forest mission. [Online]. Available: https://www.esa.int/Applications/Observing_the_Earth/FutureEO/Biomass

[24] M. Younis, S. H. C. T. Herrero, G. K. A. Moreira, A. Uematsu, Y. Sudo, R. Nakamura, Y. Chishiki, and M. Shimada, "Tandem-L instrument design and sar performance overview," in *Proc. Int. Geoscience and*

Remote Sensing Symposium (IGARSS'2014), Quebec City, Canada, July 2014.

[25] P. Focardi and P. Brown, "NISAR L-Band feed antenna tiles, preliminary design," in *2016 IEEE International Symposium on Antennas and Propagation (APSURSI)*, 2016, pp. 1379–1380.

[26] W. Imbriale, S. Gao, and L. Boccia, Eds., *Space Antenna Handbook*. John Wiley & Sons, 2012.

[27] H. L. V. Trees, *Optimum Array Processing: Part IV of Detection, Estimation, and Modulation Theory*, 1st ed. Wiley-Interscience, 2002.

[28] L. Godara, "Application of antenna arrays to mobile communications, Part II: Beam-forming and direction-of-arrival considerations," *Proceedings of the IEEE*, vol. 85, no. 8, pp. 1195–1245, Aug. 1997.

[29] S. Applebaum, "Adaptive arrays," *IEEE Transactions on Antennas and Propagation*, vol. 24, no. 5, pp. 585–598, 1976.

[30] H. Ghaemi, S. Shaffer, and S. Hensley, "Onboard digital beamforming: Algorithm and results," in *Proc. Int. Geoscience and Remote Sensing Symposium IGARSS'2014*, Quebec City, Canadaa, July 2014.

[31] C. A. Balanis, *Advanced Engineering Electromagnetics*, 2nd ed. John Wiley, 2012.

[32] J. T. Kare, "Moving receive beam method and apparatus for synthetic aperture radar," U.S. Patent 6 175 326, Jan., 2001.

[33] M. Younis and T. Bollian, *Digitale Strahlenformung für bildgebendes Radar*. Lecture notes, Institut für Hochstfrequenztechnik und Elektronik (IHE), Karlsruhe Institut für Technologie (KIT), WS 2021/2022.

[34] R. Kinsey, "Phased array beam spoiling technique," in *Proc. IEEE Int. Symposium on Antennas and Propagation*, vol. 2, Montreal, Canada, 1997, pp. 698–701.

[35] M. Villano, G. Krieger, and A. Moreira, "Advanced spaceborne SAR systems with planar antenna," in *Proc. IEEE Radar Conference*, Seattle, USA, May 2017.

[36] F. Almeida, M. Younis, G. Krieger, and A. Moreira, "An analytical error model for spaceborne SAR multichannel azimuth reconstruction," *IEEE Geoscience and Remote Sensing Letters*, vol. 15, no. 6, pp. 853–857, June 2018.

[37] T. Yang, Z. Li, Y. Liu, and Z. Bao, "Channel error estimation methods for multichannel SAR systems in azimuth," *IEEE Geoscience and Remote Sensing Letters*, vol. 10, no. 3, May 2013.

[38] R. J. Mailloux, "Phased array error correction scheme," *IEEE Electronics Letters*, vol. 29, no. 7, pp. 573–574, Apr. 1993.

[39] S. Huber, G. Krieger, F. Q. de Almeida, M. Villano, and M. Younis, "Review of state-of-the-art multichannel sar instrument architectures and processing techniques suitable for L-band SARs," German Aerospace Center, Microwaves and Radar Institute, Technical Report D2 ESA contract No. 4000116591/16/NL/FE, Jan. 2018.

[40] E. Makhoul, A. Broquetas, P. López-Dekker, J. Closa, and P. Saameno, "Evaluation of the internal calibration methodologies for spaceborne synthetic aperture radar with active phased array antennas," *IEEE Journal on Selected Topics in Applied Earth Observation and Remote Sensing*, vol. 5, pp. 909–918, June 2012.

[41] S. Horst, J. Hoffman, D. Perkovic-Martin, S. Shaffer, T. Thrivikraman, P. Yates, and L. Veilleux, "Implementation of rf circuitry for real-time digital beam-forming sar calibration schemes," in *IET International Conference on Radar Systems (Radar 2012)*, Oct. 2012.

[42] M. Younis, C. Laux, N. Al-Kahachi, P. López-Dekker, G. Krieger, and A. Moreira, "Calibration of multi-channel spaceborne SAR – challenges and strategies," in *Proc. European Conference on Synthetic Aperture Radar EUSAR'2014*, Berlin, Germany, June 2014.

[43] M. Younis, C. Laux, A. Loinger, G. Adamiuk, M. Ludwig, D. Geudtner, and G. Krieger, "Concept and performance of internal instrument calibration for multi-channel sar," in *Proc. European Conference on Synthetic Aperture Radar EUSAR'2018*, Aachen, Germany, June 2018.

[44] S. Huber, M. Younis, G. Krieger, and A. Moreira, "Error analysis for digital beamforming synthetic aperture radars: A comparison of phased array and array-fed reflector systems," *IEEE Transactions on Geoscience and Remote Sensing*, vol. 59, pp. 6314–6322, Aug. 2021.

[45] S. Bertl, P. López-Dekker, M. Younis, and G. Krieger, "Equivalency of multiple beams and multiple phase centres for digital beamforming SAR systems," in *Proc. European Conference on Synthetic Aperture Radar EUSAR'2014*, Berlin, Germany, June 2014.

[46] ——, "Along-track SAR interferometry using a single reflector antenna," *IET Radar, Sonar and Navigation*, vol. 9, Apr. 2015.

[47] P. Rosen, S. Hensley, P. Agram, E. Gurrola, L. Harcke, S. Shaffer, and C. Veeramachaneni, "Impact of gaps in the NASA-ISRO SAR mission swath," in *Proc. European Conference on Synthetic Aperture Radar EUSAR'2018*, Aachen, Germany, June 2018.

[48] M. Villano, M. Pinheiro, G. Krieger, A. Moreira, P. Rosen, S. Hensley, and C. Veeramachaneni, "Gapless imaging with the NASA-ISRO SAR (NISAR) mission: Challenges and opportunities of staggered SAR," in *Proc. European Conference on Synthetic Aperture Radar EUSAR'2018*, Aachen, Germany, June 2018.

[49] M. Younis, F. Q. de Almeida, S. Huber, M. Zonno, M. R. Cassola, S. Hensley, and G. Krieger, "The cost of opportunity for gapless imaging," in *Proc. Int. Geoscience and Remote Sensing Symposium IGARSS'19*, Yokohama, Japan, July 2019.

[50] M. Villano and M. N. Peixoto, "Characterization of nadir echoes in multiple elevation-beam SAR with constant and variable pulse repetition interval," *IEEE Transactions on Geoscience and Remote Sensing*, 2021, under review.

[51] M. Villano, G. Krieger, and A. Moreira, "Nadir echo removal in synthetic aperture radar via waveform diversity and dual-focus postprocessing," *IEEE Geoscience and Remote Sensing Letters*, vol. 15, no. 5, pp. 719–723, May 2018.

[52] S.-Y. Jeon, T. Kraus, U. Steinbrecher, G. Krieger, and M. Villano, "Experimental demonstration of nadir echo removal in SAR using waveform diversity and dual-focus postprocessing," *IEEE Geoscience and Remote Sensing Letters*, 2022.

[53] M. Younis, T. Rommel, F. Bordoni, G. Krieger, and A. Moreira, "On the pulse extension loss in digital beamforming SAR," *IEEE Geoscience and Remote Sensing Letters*, vol. 12, no. 7, pp. 1436–1440, July 2015.

[54] A. Moreira, P. Prats-Iraola, M. Younis, G. Krieger, I. Hajnsek, and K. Papathanassiou, "A tutorial on synthetic aperture radar," *IEEE Geoscience and Remote Sensing Magazine*, vol. 1, no. 1, pp. 6–43, Mar. 2013.

[55] R. K. Raney, "Considerations for SAR image quantification unique to orbital systems," *IEEE Transactions on Geoscience and Remote Sensing*, vol. 29, pp. 754–760, Sept. 1991.

[56] M. Younis and T. Bollian, "Circular orbit SAR geometry," German Aerospace Center, Microwaves and Radar Institute, Technical Note TN-RK-ST-TN7562, issue 1.6, Mar. 2022.

[57] N. Gebert, G. Krieger, and A. Moreira, "Digital beamforming on receive: Techniques and optimization strategies for high-resolution wide-swath SAR imaging," *IEEE Transactions on Aerospace and Electronic Systems*, vol. 45, pp. 564–592, 2009.

[58] G. Krieger, N. Gebert, and A. Moreira, "Unambiguous SAR signal reconstruction from non-uniform displaced phase centre sampling," *IEEE Geoscience and Remote Sensing Letters*, vol. 1, no. 4, pp. 260–264, Oct. 2004.

[59] ——, "Multidimensional waveform encoding: A new digital beamforming technique for synthetic aperture radar remote sensing," *IEEE Transactions on Geoscience and Remote Sensing*, vol. 46, no. 1, pp. 31–46, Jan. 2008.

[60] S. Huber, M. Younis, G. Krieger, A. Patyuchenko, and A. Moreira, "Spaceborne reflector SAR systems with digital beamforming," *IEEE Transactions on Aerospace and Electronic Systems*, vol. 48, no. 4, pp. 3473–3493, Oct. 2012.

[61] M. Younis and W. Wiesbeck, "SAR with digital beamforming on receive only," in *Proc. Int. Geoscience and Remote Sensing Symposium IGARSS'99*, vol. 3, Hamburg, Germany, June 1999, pp. 1773–1775.

[62] I. Sikaneta, C. Gierull, and D. Cerutti-Maori, "Optimum signal processing for multichannel SAR: With application to high-resolution wide-swath imaging," *IEEE Transactions on Geoscience and Remote Sensing*, vol. 52, no. 10, pp. 6095–6109, Oct. 2014.

[63] C. E. Shannon, "Communication in the presence of noise," *Proceedings of the Institute of Radio Engineers*, vol. 37, no. 1, pp. 10–21, 1949.

[64] "Calibration and data reduction for digital beam forming instruments – technical reports," European Space Agency (ESA/ESTEC), Tech. Rep. ESA/ESTEC Contract Nr. 4000117363/16/NL/FE, Dec. 2018.

[65] M. Younis, "NESZ-formulation for planar multi-channel SAR," German Aerospace Center, Microwaves and Radar Institute, Technical Note HR-RK-TN MY101, issue 2.3, Apr. 2019.

[66] M. Villano, "Staggered synthetic aperture radar," Ph.D. dissertation, DLR-Forschungsbericht DLR-FB-2016-16, Mar. 2016.

[67] F. Almeida, "Multichannel staggered SAR for high-resolution wide-swath imaging," Ph.D. dissertation, DLR-Forschungsbericht DLR-FB-2018-3, Dec. 2017.